



## On the Response of Polarimetric GNSS-Reflectometry to Sea Surface Roughness

Downloaded from: <https://research.chalmers.se>, 2021-12-11 21:10 UTC

Citation for the original published paper (version of record):

Hoseini, M., Semmling, M., Nahavandchi, H. et al (2021)

On the Response of Polarimetric GNSS-Reflectometry to Sea Surface Roughness

IEEE Transactions on Geoscience and Remote Sensing, 59(9): 7945-7956

<http://dx.doi.org/10.1109/TGRS.2020.3031396>

N.B. When citing this work, cite the original published paper.

©2021 IEEE. Personal use of this material is permitted.

However, permission to reprint/republish this material for advertising or promotional purposes or for creating new collective works for resale or redistribution to servers or lists, or to reuse any copyrighted component of this work in other works must be obtained from the IEEE.

# On the Response of Polarimetric GNSS-Reflectometry to Sea Surface Roughness

Mostafa Hoseini<sup>1</sup>, Maximilian Semmling, Hossein Nahavandchi<sup>2</sup>, Erik Rennspiess,  
Markus Ramatschi, Rüdiger Haas<sup>3</sup>, Joakim Strandberg<sup>4</sup>, and Jens Wickert<sup>5</sup>

**Abstract**—Reflectometry of Global Navigation Satellite Systems (GNSS) signals from the ocean surface has provided a new source of observations to study the ocean–atmosphere interaction. We investigate the sensitivity and performance of GNSS-Reflectometry (GNSS-R) data to retrieve sea surface roughness (SSR) as an indicator of sea state. A data set of one-year observations in 2016 is acquired from a coastal GNSS-R experiment in Onsala, Sweden. The experiment exploits two sea-looking antennas with right- and left-hand circular polarizations (RHCP and LHCP). The interference of the direct and reflected signals captured by the antennas is used by a GNSS-R receiver to generate complex interferometric fringes. We process the interferometric observations to estimate the contributions of direct signals and reflections to the total power. The power estimates are inverted to the SSR using the state-of-the-art model. The roughness measurements from the RHCP and LHCP links are evaluated against match-up wind measurements obtained from the nearest meteorological station. The results report on successful roughness retrieval with overall correlations of 0.76 for both links. However, the roughness effect in LHCP observations is more pronounced. The influence of surrounding complex coastlines and the wind direction dependence are discussed. The analysis reveals that the winds blowing from land have minimal impact on the roughness due to limited fetch. A clear improvement of roughness estimates with an overall correlation of 0.82 is observed for combined polarimetric observations from the RHCP and LHCP links. The combined observations can also improve the sensitivity of GNSS-R measurements to the change of sea state.

**Index Terms**—Global Navigation Satellite Systems (GNSS)-Reflectometry, polarimetric observations, sea state, sea surface roughness (SSR).

Manuscript received July 26, 2020; revised September 9, 2020; accepted October 6, 2020. Date of publication November 2, 2020; date of current version August 30, 2021. This work was supported by the Norwegian University of Science and Technology (NTNU), under Grant 81771107. (Corresponding author: Mostafa Hoseini.)

Mostafa Hoseini and Hossein Nahavandchi are with the Department of Civil and Environmental Engineering, Norwegian University of Science and Technology, 7491 Trondheim, Norway (e-mail: mostafa.hoseini@ntnu.no).

Maximilian Semmling is with the Institute for Solar-Terrestrial Physics, German Aerospace Center (DLR-SO), D-17235 Neustrelitz, Germany.

Erik Rennspiess is with the Institute of Geodesy and Geoinformation Science, Technische Universität Berlin, 10623 Berlin, Germany.

Markus Ramatschi is with the Department of Geodesy, German Research Center for Geosciences (GFZ), 14473 Potsdam, Germany.

Rüdiger Haas and Joakim Strandberg are with the Department of Space, Earth and Environment, Chalmers University of Technology, 43992 Gothenburg, Sweden.

Jens Wickert is with the Department of Geodesy, German Research Center for Geosciences (GFZ), 14473 Potsdam, Germany, and also with the Institute of Geodesy and Geoinformation Science, Technische Universität Berlin, 10623 Berlin, Germany.

Digital Object Identifier 10.1109/TGRS.2020.3031396

## I. INTRODUCTION

THE characterization and monitoring of sea surface roughness (SSR) are important for understanding air–sea interactions. This parameter is considered as one of the indicators of the sea state. The difficulty of making direct SSR measurements due to the complexity and random behavior of sea surface fluctuations has cleared the way for remote sensing techniques [1]. A robust observation resource of SSR can be acquired from the reflectometry of the Global Navigation Satellite Systems (GNSS) signals.

The GNSS-Reflectometry (GNSS-R) is an all-weather operating technique offering high temporal resolution observations based on low-cost passive instrumentation. Spaceborne observations of the surface roughness variations can be related to the near-surface wind stress [2] and used for the estimation of wind speed [3]. The anomalies of surface roughness over mesoscale ocean eddies can reveal the presence of these oceanic features and the ongoing air–sea interaction [4].

The ground-based GNSS-R setup has been used in several experimental campaigns for sea state observations. Different observables are proposed to retrieve SSR or Significant Wave Height (SWH) as descriptors of the sea state or predictors of wind speed. The complex delay Doppler Maps (DDMs) produced from the processing of GNSS reflected signals [5] can provide several observables. The waveforms extracted from the DDMs can be fit to a wind-dependent model to estimate the speed [2]. The volume of the DDMs can be normalized and directly connected to the sea state [6].

Interferometric observations of the superimposed direct and reflected signals can be utilized for the sea state estimation. The coherence time of the observed signal can be modeled and related to the ratio of SWH and mean wave period [7]. Variability of the sea state can be derived from the analysis of power loss due to the roughness. The latter approach is considered in this article for the SSR estimation.

The nature of GNSS signals at the reflection is subject to polarization change described by the Fresnel equations. Therefore, the incoming direct signals with right-hand circular polarization (RHCP) produce composite reflected signals, including left-hand circular polarization (LHCP) and RHCP components. This phenomenon offers the opportunity of making polarimetric observations. The reflectometry receivers can be fed by RHCP or LHCP antennas to perform the GNSS-R measurements. The use of polarimetric observations for different applications has been considered in several earlier studies [8]–[11].

This study aims at investigating the performance of GNSS-R observations with RHCP, LHCP, and a combination of them in the SSR estimations. To this end, we use a long-term data set from a coastal GNSS-R experiment equipped with RHCP and LHCP antennas. We analyze the impact of the surface roughness on the interferometric observations of the Global Positioning System (GPS) signals collected by each of the antennas during different sea states. The GNSS-R setup used in this study together with the data set is described in Section II. The processing flow from receiving signals at the antennas to deriving the surface roughness, i.e., the geophysical parameter of interest, is explained in Section III. The processing results are discussed in Section IV. Section V provides concluding remarks.

## II. DATA

The data set used in this study includes one-year observations of a ground-based coastal GNSS-R experiment at the Onsala space observatory ( $57.393^\circ N$ ,  $11.914^\circ E$ ) in Sweden. The station uses a metal structure that is placed on a cliff at about 3 m above the sea level to accommodate the antennas. A zenith-looking antenna is used for tracking direct signals. Sea surface reflections are intercepted by two sea-looking antennas with RHCP and LHCP designs. The sea-looking antennas have a tilt angle of about  $98^\circ$  with respect to the zenith, i.e., slightly down-looking. These antennas are, respectively, optimized for receiving copolarized (CPo) and cross-polarized (XPo) reflected signals by analogy with the incoming direct RHCP signals. The boresight of the reflectometry antennas is fixed at about  $150^\circ$  azimuth angle to overlook the sea. Fig. 1 shows the location of the station along the Sweden coastlines, as well as the top and side views of the setup.

A GNSS Occultation, Reflectometry, and Scatterometry (GORS) receiver [12] is used at the station providing up to four input links. The first link is connected to the master channel of the receiver to track the direct signals of the satellites. The other links are connected to slave channels for reflectometry purposes. The receiver can process GPS signals and delivers raw data streams at the sampling rate of 200 Hz.

Direct and reflected signals from the GPS satellites in view are captured by the antennas and fed to the master and slave channels of the receiver. The receiver tracks the satellites by cross-correlating a replica of their pseudorandom noise (PRN) codes with the signals received from the master link. Similar cross-correlations are computed within the slave channels. The receiver can be instructed to use different delay and Doppler values in the slave channels. These values are relative with respect to the master channel. The geometrical configuration of the setup at Onsala station demands negligible relative delay and Doppler values. Therefore, the relative delay and Doppler values for all of the tracked satellites are set to zero. The correlation sums are provided by the receiver at In-phase and Quadrature (I/Q) levels. The 200-Hz data stream is downsampled to 0.1 Hz by 10-second integration. The downsampled observations suffice the required temporal resolution for the



Fig. 1. (Top Left) Top view of the Onsala GNSS-R station located in southern Sweden. (Top Right) Nearby coastlines. (Bottom Left) Close eastward. (Bottom Right) Downward photographs from the antennas and the setup structure. The GNSS-R station is marked with a yellow diamond, and the yellow circle shows the location of the nearby tide gauge station. The orange arrow indicates the boresight of the reflectometry antennas.

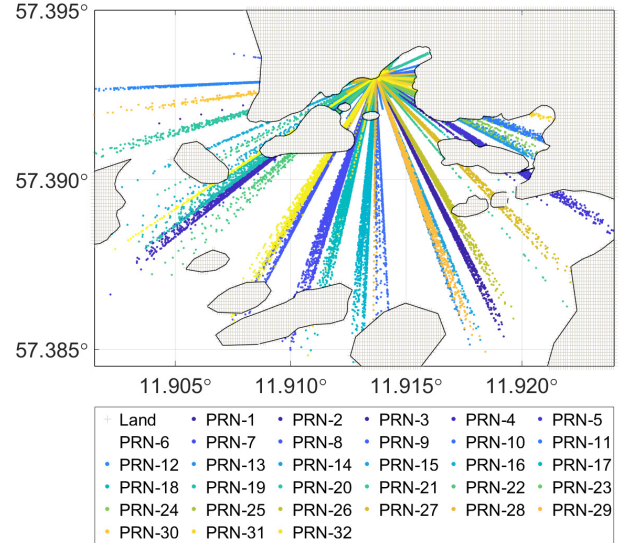


Fig. 2. Distribution of the reflection points of the GPS satellites over the sea surface.

processing, due to the small height difference between the reflectometry antennas and the sea surface [according to (4)].

The data set used in this study covers the period from January to December 2016. On average, about 44 reflection events per day from different GPS satellites were recorded and used for the analysis. Fig. 2 shows the spatial spread of the reflection tracks of the satellites over the sea surface. The selected region of the sea surface encompasses specular points with corresponding elevation angles of up to  $55^\circ$ .



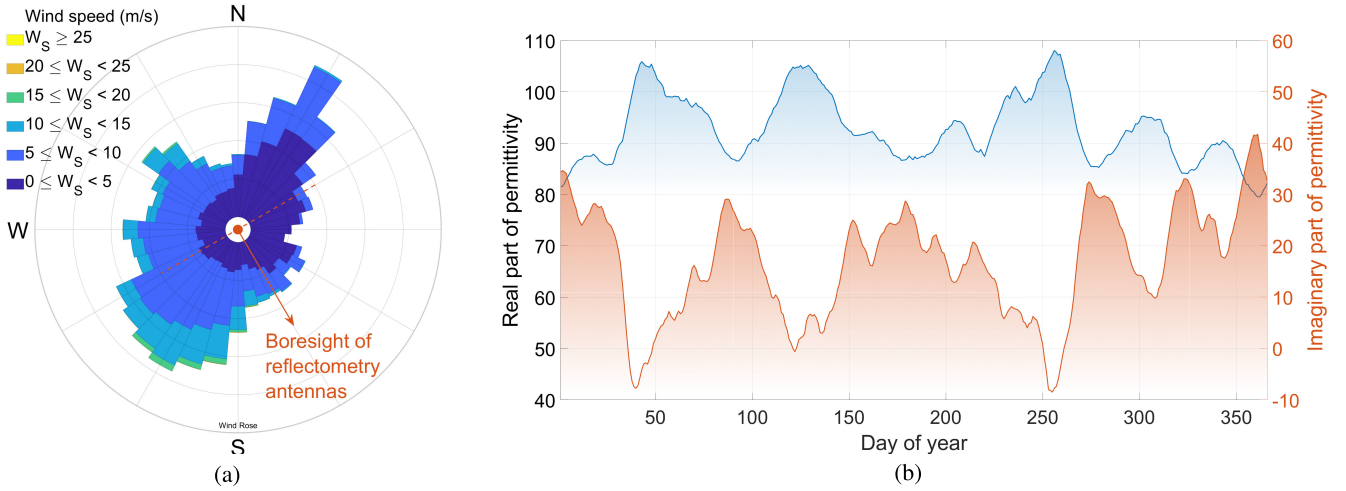


Fig. 3. Overview of the ancillary data at Onsala station in 2016. (a) Distribution of wind speeds with respect to wind directions (bin size for the speeds: 5 m/s and sector size for the directions:  $10^\circ$ ). (b) Seawater relative permittivity.

The reflectometry observations in the main data set are coupled with available ancillary information. Hourly measurements of wind speed and direction are acquired from a nearby meteorological station. Distribution of wind direction and the range of wind speeds in 2016 are shown in Fig. 3(a). Sea level anomalies with a resolution of 1 min are also measured by a tide gauge station, which is marked with a yellow circle to the east of the reflectometry station in Fig. 1.

To improve the accuracy of the roughness estimates, relative permittivity values are calculated and used within the processing. To this end, we use a model developed by [13] to describe the dielectric constant of seawater at L-band frequency as a function of salinity and temperature. The model utilizes a third-order polynomial that is trained using a set of accurate measurements at the frequency of 1.413 GHz [14]. The required water temperature values are obtained from the meteorological station. Due to the lack of *in situ* salinity observations, we use daily averages based on nine years of historical records (2001–2009) from another station that is about 29 km away. The estimated seawater permittivity at the Onsala station in 2016 is shown in Fig. 3(b).

### III. METHOD

The method used in this study is based on the analysis of interference fringes caused by the superposition of the direct and reflected GNSS signals. The superimposed signals generate a compound electromagnetic field. The field is intercepted by the antennas and processed by the receiver to generate output streams in the form of I/Q components. The receiver output can be represented by a complex time series as

$$E = I_{\text{int}} + i Q_{\text{int}} \quad (1)$$

where  $E$  denotes the complex vector form and  $I_{\text{int}}$  and  $Q_{\text{int}}$  are, respectively, the I and Q components of the interferometric signal from the receiver output. We process these I/Q correlation sums (data level 0) to extract the power of direct and reflected signals and combine them into three power ratios (data level 1). The estimated power ratios are then inverted to

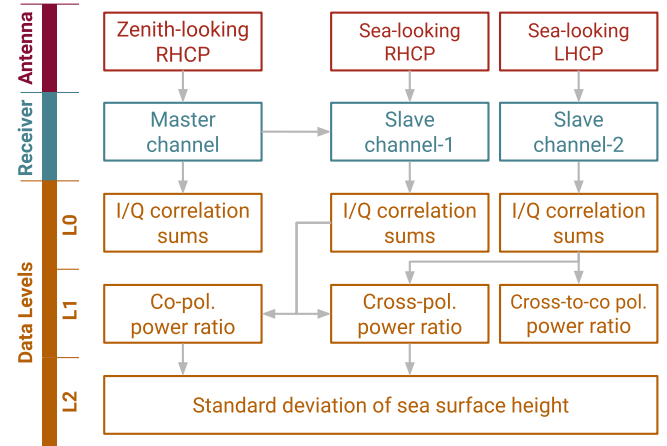


Fig. 4. Procedure of data processing from the raw interferometric observations at in-phase and quadrature (I/Q) levels to the final data product of SSR.

SSR (data level 2) using a geophysical model function. The following description provides detailed information about the processing procedure shown in Fig. 4.

The observed signal contains contributions from the direct and reflected signals and can be written, cf. [15], as

$$I_{\text{int}} + i Q_{\text{int}} = (I_{\text{dir}} + i Q_{\text{dir}}) + (I_{\text{ref}} + i Q_{\text{ref}}) \quad (2)$$

with the subscript *dir* and *ref* denoting the components of the direct and reflected signals, respectively. Fig. 5 demonstrates an example of the receiver output from the two slave antennas. As can be seen in the figure, both the I and Q components exhibit long- and short-term variations that originated from different contributors. The long-term slowly varying trend is governed by variations of the direct signal amplitude, antenna gain pattern, and the baseline between the master and slave antennas. The prominent high-frequency oscillations at the beginning and the end of the time series shown in the figure are the interferometric fringes. These fringes are extracted from the compound signal and are investigated in our analysis. The amplitude of the interferometric oscillations is



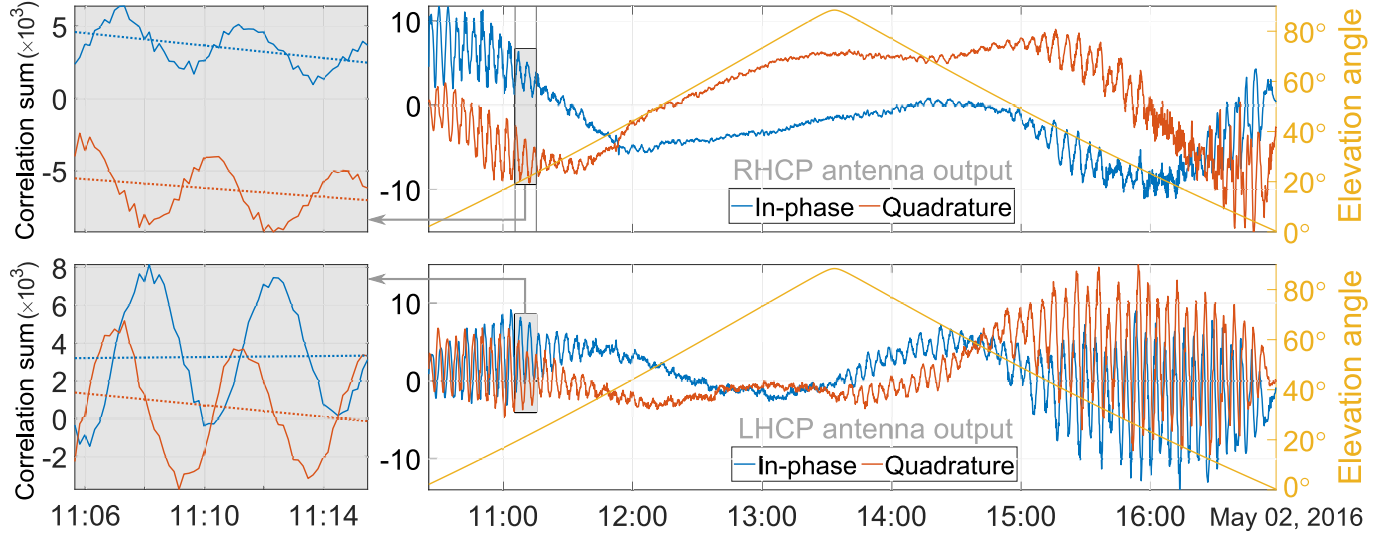


Fig. 5. Examples of in-phase (I) and quadrature (Q) correlation sums of GPS PRN 12 from the two sea-looking antennas used for the reflectometry. The top figures are related to the copolarization link (RHCP antenna), and the bottom figures show the data from the cross-polarization link (LHCP antenna). The selected segments shown on the left figures are used for estimating the power of direct and reflected signals. The first-order polynomial fits in these segments (dotted lines) indicate the contribution of the direct signals.

the main parameter of interest in the analysis. This parameter is controlled by several factors. The main factors are the strength of the incoming direct signal, antenna gain, satellite elevation angle, dielectric constant of seawater, and SSR. The methodology of this study is focused on estimating the effect of the SSR. Therefore, the effects of the other factors are either modeled or mitigated within the processing flow.

To decompose the compound signal, we estimate and utilize the frequency of the interference fringes. This frequency is the Doppler shift caused by the different traveling paths of the direct and reflected signals and can be calculated, cf. [15], by

$$\delta f = \frac{1}{\lambda} \frac{d(\delta \rho)}{dt}, \quad \delta \rho = \rho_{\text{ref}} - \rho_{\text{dir}} \quad (3)$$

where  $\delta f$  is the Doppler shift,  $\rho_{\text{dir}}$  and  $\rho_{\text{ref}}$  are lengths of the paths traveled by the direct and reflected signals, respectively, and  $\lambda$  is the wavelength of the signal carrier. It should be noted that another Doppler shift could also be found in the observations due to the baseline [16]. However, the frequency of the latter shift in the Onsala setup is much lower compared to the interferometric frequency and would not noticeably affect the power retrievals. We use the period of interferometric oscillations to split the I/Q time series into successive segments from which the power of direct and reflected signals can be estimated [15]. The reciprocal value of this period, i.e., the frequency  $\delta f$ , is related to the geometry of reflection (see Fig. 6) by

$$\begin{aligned} \delta \rho &= 2 \delta H \sin(e) \\ \delta f &= \frac{2 \delta H \cos(e)}{\lambda} \frac{de}{dt} \end{aligned} \quad (4)$$

where  $e$  is the elevation angle of the tracked satellite and  $\delta H$  is the height difference between the phase center of the slave antennas and sea level. From a fast Fourier transform (FFT)

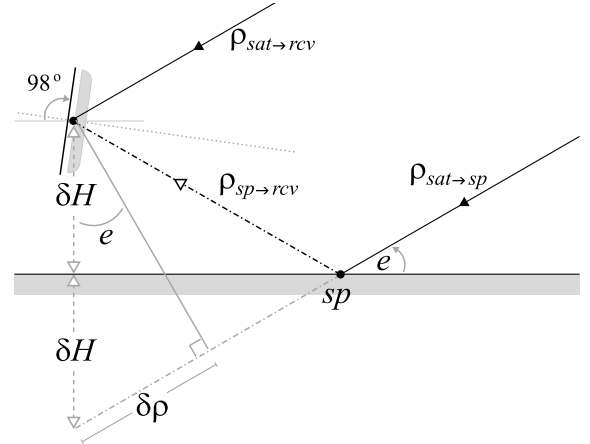


Fig. 6. Geometry of specular reflection and the path difference between the direct and reflected signals.

analysis, the dominant interferometric period in the observations is estimated to be around 5 min. Therefore, we use a time interval of 10 min for the segmentation to include two complete interferometric periods in each segment.

The separated segments of I/Q samples from the slave channels are independently processed to retrieve the contributions of the direct and reflected signals. The first-order polynomial is used to model the long term variations [see Fig. 5 (Left)]. These variations are attributed to the direct signal and can be used to estimate the corresponding power

$$\hat{P}_{\text{dir}} = \text{avg}(|\hat{I}_{\text{dir}} + i \hat{Q}_{\text{dir}}|^2) \quad (5)$$

where avg denotes the average function and  $\hat{P}_{\text{dir}}$  is the estimate of the direct signal power over the segment. The variables  $\hat{I}_{\text{dir}}$  and  $\hat{Q}_{\text{dir}}$  are, respectively, the modeled I and Q amplitudes using the first-order polynomial and can be used to retrieve

the contribution of the reflected signal ( $\hat{I}_{\text{ref}}$  and  $\hat{Q}_{\text{ref}}$ ) by

$$\begin{aligned}\hat{I}_{\text{ref}} &= \hat{I}_{\text{int}} - \hat{I}_{\text{dir}} \\ \hat{Q}_{\text{ref}} &= \hat{Q}_{\text{int}} - \hat{Q}_{\text{dir}}.\end{aligned}\quad (6)$$

The retrieved I/Q contributions of the reflected signal over each segment are processed using a Lomb–Scargle periodogram (LSP) to estimate the power of reflected signals in a similar approach used by [17] and [15]. According to (4), a change in the height difference ( $\delta H$ ) results in a change in the interferometric frequency. The height difference between the antennas and the sea level over each segment is obtained from the tide gauge measurements. Therefore, with the knowledge of the satellite elevation angle from orbit information, we can precisely extract the power of reflected signals ( $\hat{P}_{\text{ref}}$ ) from the periodogram. The estimated powers of the direct and reflected signals from the described procedure can be now related to the main involving factors through [18]

$$\begin{aligned}\hat{P}_{\text{dir}} &= G_{\text{dir}} P_0 \\ \hat{P}_{\text{ref}} &= G_{\text{ref}} |R|^2 S^2 P_0\end{aligned}\quad (7)$$

with  $P_0$  being the power of the incoming signal at the antenna (and at the specular point),  $G$  the antenna gain factor,  $R$  the complex-valued Fresnel reflection coefficient, and  $S$  a dampening factor due to the reflecting surface roughness. The power loss due to insufficient delay-Doppler tracking of reflected signal [15] is ignored since the difference of the delay/Doppler values for the reflected and direct signals are negligible in the Onsala configuration.

The Fresnel reflection coefficient describes polarization states of the reflected signals. The RHCP polarization of the incoming signal is altered during the reflection. The reflected signal includes both RHCP and LHCP polarizations. The proportion of each part in the reflected signal is estimated using Fresnel copolarization and cross-polarization coefficients. Both of the two coefficients are functions of elevation angle of the incoming signal and the permittivity of the reflecting medium [15], [19]

$$\begin{aligned}R_{\parallel} &= \frac{\epsilon_{\text{sea}} \sin e - \sqrt{\epsilon_{\text{air}} \epsilon_{\text{sea}} - (\epsilon_{\text{air}} \cos e)^2}}{\epsilon_{\text{sea}} \sin e + \sqrt{\epsilon_{\text{air}} \epsilon_{\text{sea}} - (\epsilon_{\text{air}} \cos e)^2}} \\ R_{\perp} &= \frac{\epsilon_{\text{air}} \sin e - \sqrt{\epsilon_{\text{air}} \epsilon_{\text{sea}} - (\epsilon_{\text{air}} \cos e)^2}}{\epsilon_{\text{air}} \sin e + \sqrt{\epsilon_{\text{air}} \epsilon_{\text{sea}} - (\epsilon_{\text{air}} \cos e)^2}}\end{aligned}\quad (8)$$

where  $R_{\parallel}$  and  $R_{\perp}$  denote, respectively, the reflections with the polarization parallel to incidence plane and perpendicular to it. These coefficients can be combined to yield copolarization ( $R^{\text{co}}$ ) and cross-polarization ( $R^{\text{cross}}$ ) forms of the Fresnel coefficients [19]

$$\begin{aligned}R^{\text{co}} &= \frac{1}{2}(R_{\parallel} + R_{\perp}) \\ R^{\text{cross}} &= \frac{1}{2}(R_{\parallel} - R_{\perp}).\end{aligned}\quad (9)$$

Fig. 7 depicts the Fresnel coefficients using the estimated permittivity of seawater at the Onsala station. The shaded areas show the slight variations of the coefficients based on the variations of the permittivity on different days of the year.

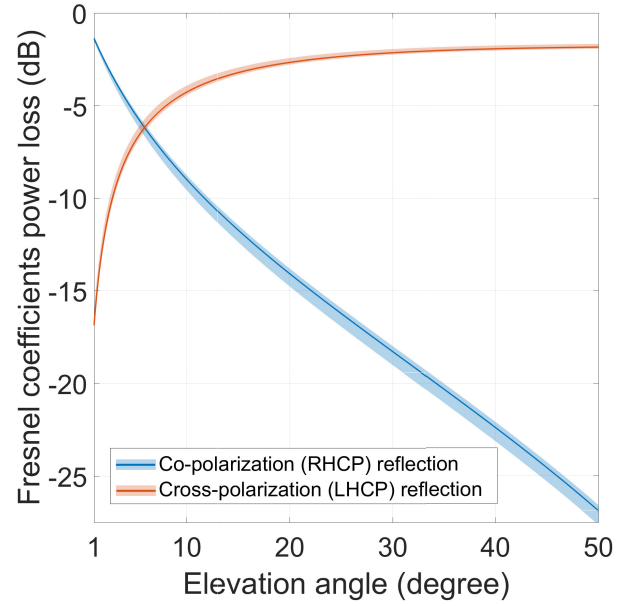


Fig. 7. Fresnel reflection coefficients calculated using the permittivity of seawater at the Onsala GNSS-R station. Based on the average permittivity, the blue and orange lines denote the magnitude of the copolarization and cross-polarization reflection coefficients in decibels (dB), respectively. The spread of the shaded areas shows the distribution of the coefficients based on the variations of local seawater permittivity shown in Fig. 3(b).

The factor  $S$  in (7) is a model that relates the standard deviation of sea surface height ( $\sigma$ ) as a measure of surface roughness to the resultant power loss. The model is independent of the polarization and reads [18]

$$S = \exp\left(-\frac{1}{2} \frac{(2\pi)^2}{\lambda^2} \sigma^2 \sin^2 e\right). \quad (10)$$

We use the introduced Fresnel equations and the roughness model to invert the observed powers to the SSR measurements. The unknown parameter  $P_0$  can be canceled out by forming the following power ratios:

$$\begin{aligned}L^c &= \frac{\hat{P}_{\text{ref}}^{\text{co}}}{\hat{P}_{\text{dir}}^{\text{co}}} = \frac{G_{\text{ref}}}{G_{\text{dir}}} |R^{\text{co}}|^2 S_c^2 \\ L^x &= \frac{\hat{P}_{\text{ref}}^{\text{cross}}}{\hat{P}_{\text{dir}}^{\text{co}}} = \frac{G_{\text{ref}}}{G_{\text{dir}}} |R^{\text{cross}}|^2 S_x^2.\end{aligned}\quad (11)$$

The variables  $L^c$  and  $L^x$  are, respectively, copolarization and cross-polarization power ratios that are our level-1 observables through which we estimate the SSR.  $L^c$  and  $L^x$  are estimated using the power of reflected signals, i.e.  $\hat{P}_{\text{ref}}^{\text{co}}$  and  $\hat{P}_{\text{ref}}^{\text{cross}}$ , which are derived from the RHCP and LHCP slave antennas, respectively. Note that, for both of the ratios, the reference power in (11),  $\hat{P}_{\text{dir}}^{\text{co}}$ , is retrieved from the sea-looking RHCP antenna. Besides, cross-to-copolarization power ratio  $L^{x2c}$  that is the ratio of  $L^x$  to  $L^c$  reads

$$L^{x2c} = \frac{\hat{P}_{\text{ref}}^{\text{cross}}}{\hat{P}_{\text{ref}}^{\text{co}}} = \frac{|R^{\text{cross}}|^2 S_x^2}{|R^{\text{co}}|^2 S_c^2}. \quad (12)$$

We invert the calculated power ratios to the standard deviation of sea surface height. The inversion is independently done for  $L^c$ ,  $L^x$ , and  $L^{x2c}$  through solving an optimization problem. For this purpose, all the power ratios from different

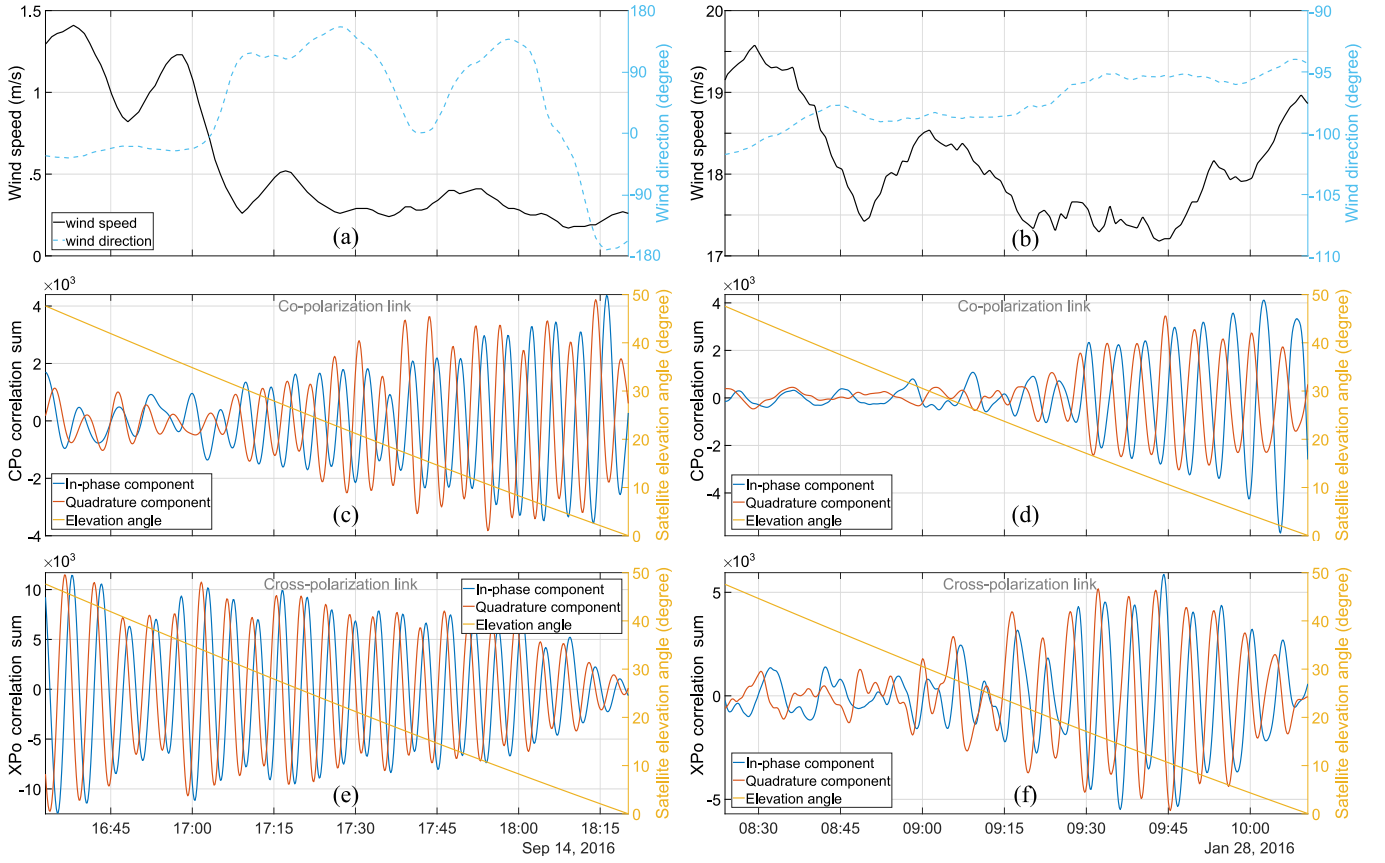


Fig. 8. Exemplary case of the impact of wind speed on the amplitude of copolarization (CPo) and cross-polarization (XPo) reflectometry observations from the GPS satellite PRN 1. The observations are associated with a similar range of the satellite elevation angles on two different days. The left and right columns are associated with periods of low and high wind speeds, respectively. (a) and (b) Direction and speed of the wind. Figures (c) and (d) In-phase and quadrature components of the copolarization observations that are recorded from the RHCP sea-looking antenna. (e) and (f) In-phase and quadrature components of the cross-polarization observations that are recorded from the LHCP sea-looking antenna. The reduced intensity of signals on the right figures (d) and (f) during wind speed of about 18 m/s is remarkable compared with the significantly higher signal amplitudes shown in (c) and (e) during the wind speed of about 1 m/s.

satellites over a common time interval are grouped and used to minimize the following cost function:

$$\min_{\sigma} \sum_i (L_i - |R_i|^2 S^2)^2 \quad (13)$$

with  $\min$  being the minimum function and the index  $i$  referring to all of the observations falling in a common time interval.

#### IV. RESULTS AND DISCUSSION

We apply the described method to the observed amplitude anomalies of interferometric signals to measure SSR variations. In the absence of *in situ* roughness estimates, we use the wind speed and wind direction for the analysis.

An exemplary case of the amplitude anomaly is shown in Fig. 8. The figure demonstrates the copolarization and cross-polarization reflection amplitudes at two different wind speeds during the setting period of the GPS satellite PRN 1. The left column in the figure shows the I/Q components of the reflected signal during a low wind speed period. A drastic reduction of the signal amplitude due to a significantly higher wind speed can be seen in the right column graphs.

The comparison of the amplitudes from the two links in Fig. 8(c) and (d) with those in Fig. 8(e) and (f) reports

much more powerful cross-polarization reflections. Moreover, the magnitudes of the in-phase and quadrature components in the cross-polarization link are varying consistently over time. On the contrary, the relatively weaker copolarization reflections exhibit inconsistencies between the magnitudes of the I and Q components. A prominent case of the inconsistency occurs at about 17:40 in Fig. 8(c) where the wind field shows an abrupt direction change. Such inconsistency between I and Q magnitudes appears in a fading of signal amplitude linked with a short-term loss of phase coherence. Hence, abrupt changes in the wind field could result in a loss of phase coherence.

The results of processing for about  $7 \times 10^4$  segments of 10-min intervals in 2016 are summarized in Fig. 9. The figure shows the distribution of the observed power ratios against the elevation angle of the satellite. The estimates of power ratios are overlaid with the roughness model, i.e., (10), with different  $\sigma$  values. A comparison of the distributions with the model predictions suggests an overall agreement for all of the power ratios.

The distribution of the copolarization power ratios in Fig. 9(a) is mainly scattered around the lowest roughness models, i.e.,  $\sigma \leq 10$  cm. This can be an indicator of



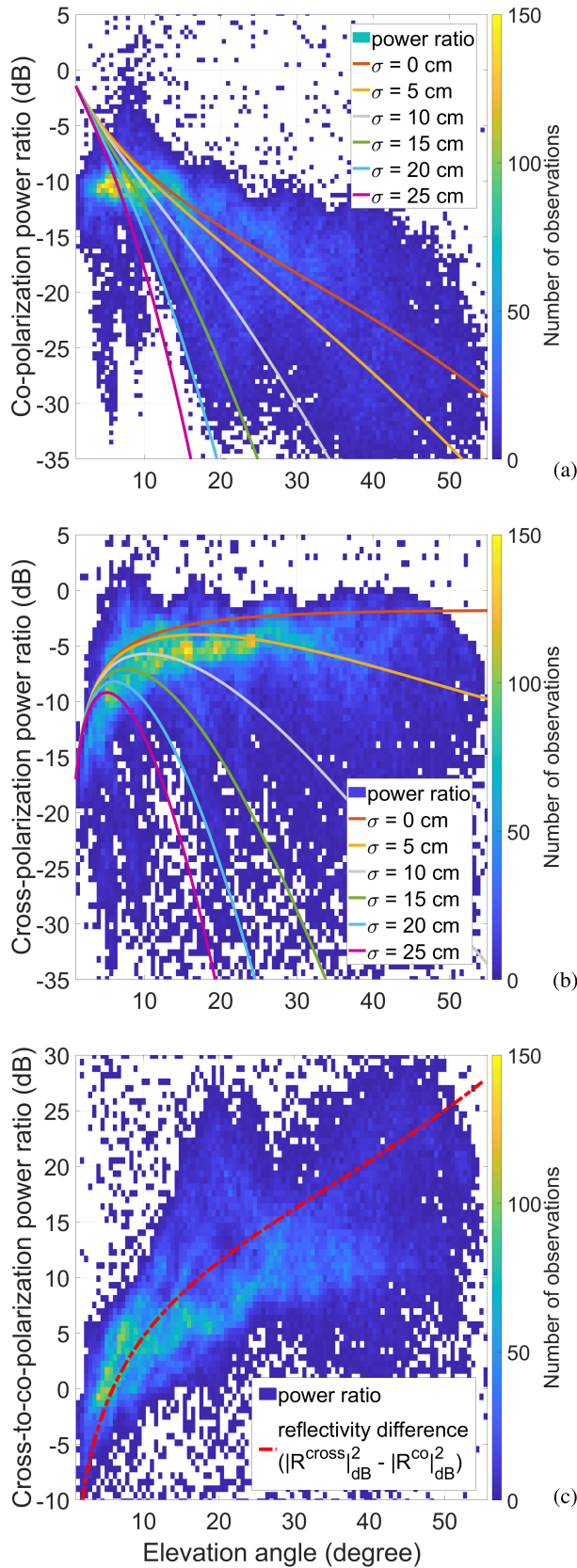


Fig. 9. Distribution of the estimated power ratios from the sea-looking antennas. (a) Copolarization (RHCP). (b) Cross-polarization (LHCP). (c) Cross-to-copolarization. The solid lines are model predictions based on different values of standard deviation of sea surface height ( $\sigma$ ). The dashed-dotted line is the ratio of cross-to-copolarization reflectivity.

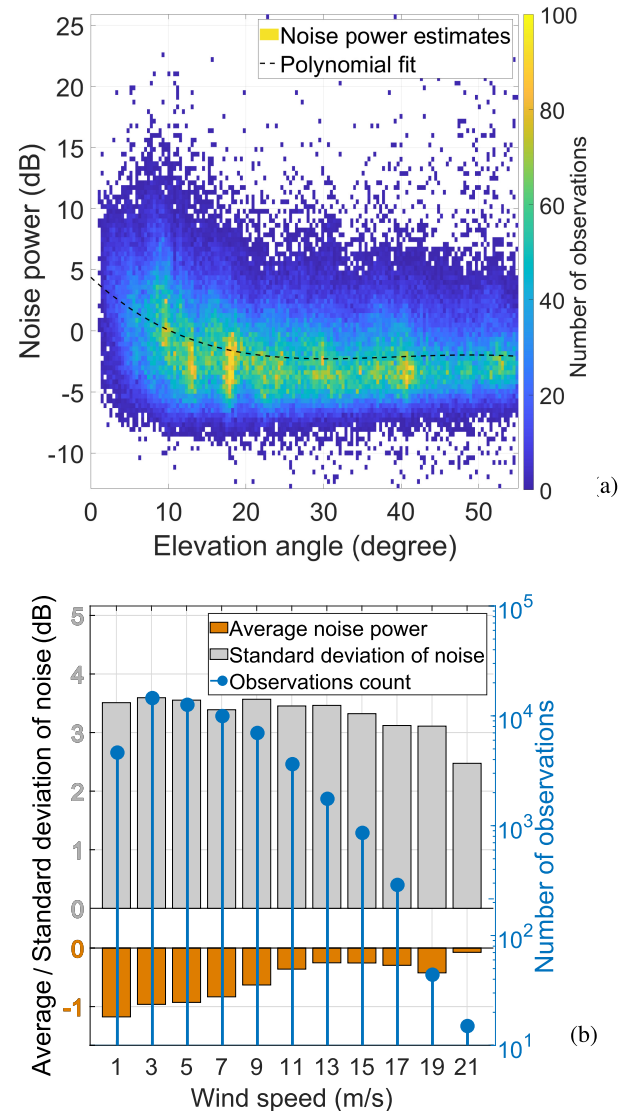


Fig. 10. (a) Distribution of noise power estimates against the elevation angle of incoming signals. (b) Average and standard deviation of the noise power in different wind speeds.

less sensitivity of copolarization observations to the SSR. Moreover, two noticeable biases with respect to the model predictions can be observed for the ratios in Fig. 9(a). The first bias occurs at very low elevation angles. This bias could be related to the performance of the roughness model, i.e., over these angles, the model underestimates the impact of the roughness for copolarization power ratios. Interestingly, at the elevation angles below  $5^\circ$  where the impact of roughness is expected to almost disappear, the ratios still reflect the impact of high sea states.

The estimated power ratios from the cross-polarization link are shown in Fig. 9(b). These ratios manifest a wider spread around the models with different values of  $\sigma$  compared to the copolarization power ratios. The presence of positive power ratios at elevation angles about  $8^\circ$  for both copolarization and cross-polarization power ratios can be related to the antenna gain. The antenna gain pattern used in our processing is

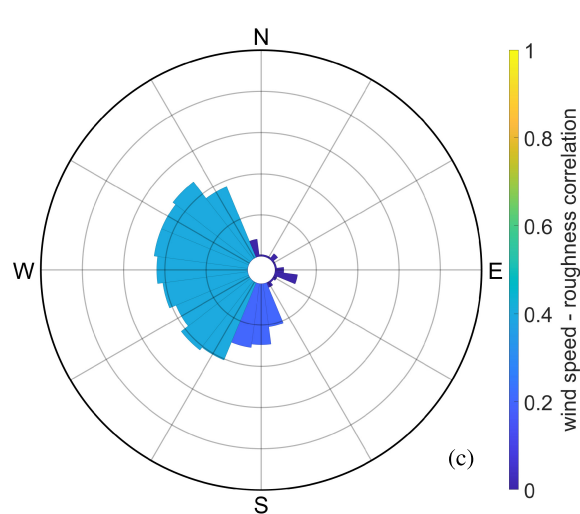
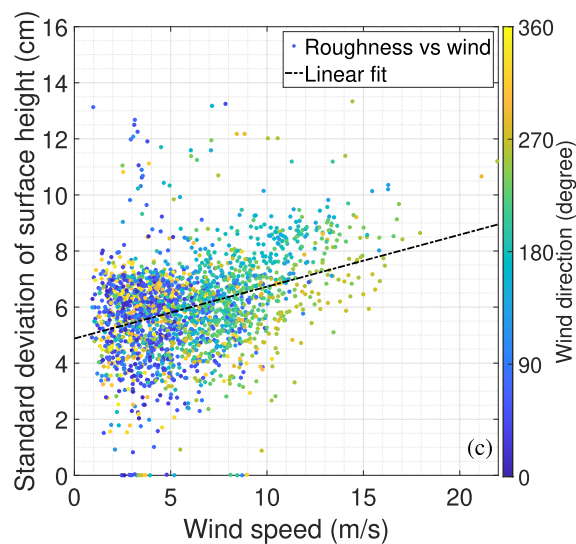
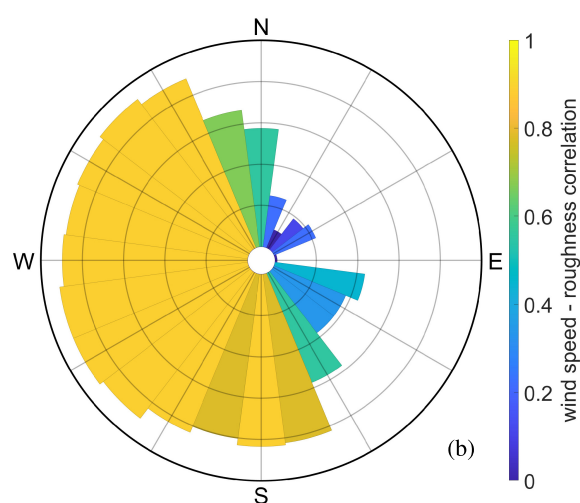
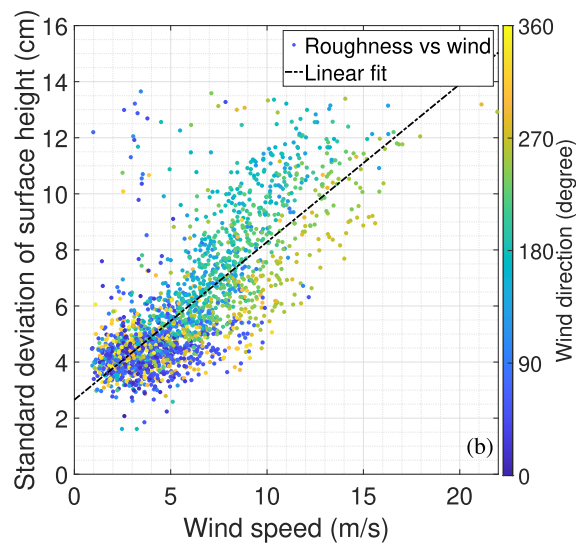
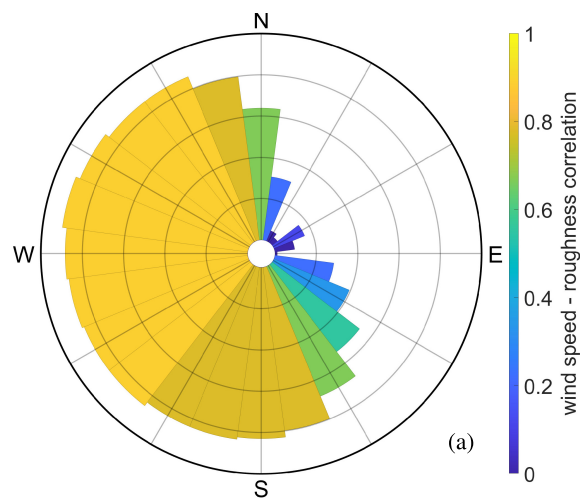
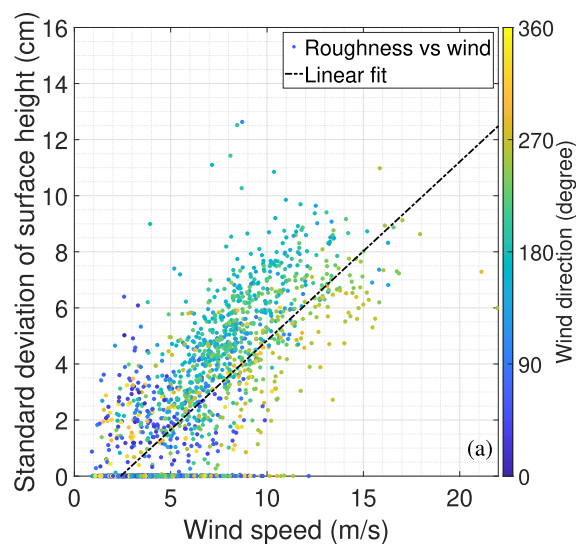


Fig. 11. Results of the roughness retrievals based on the one-year GNSS-R measurements in 2016 estimated from: (a) copolarization, (b) cross-polarization, and (c) cross-to-copolarization power ratios.

Fig. 12. Sensitivity of roughness measurements to wind direction. The correlation of wind speeds with (a) copolarization, (b) cross-polarization, and (c) cross-to-copolarization roughness retrievals is shown as a function of wind direction.



Fig. 13. Demonstration of the impact of wind direction and the complex coastlines on the SSR over different areas nearby the Onsala GNSS-R station. The station is shown by a yellow diamond symbol.

estimated based on the interpolation of a few discrete gain values provided by the antenna datasheet. The gain pattern is assumed to be symmetric in terms of the azimuth angle. At the boresight of the tilted antennas, the specularly reflected signals from the satellites at elevation angles around  $8^\circ$  (the dotted gray line in Fig. 6) are collected at the highest possible gain. At this configuration, the gain can dramatically change with the change of the satellite azimuth angle. Therefore, possible uncertainties within the interpolated gain pattern could produce positive power ratios.

Fig. 9(c) shows the distribution of cross-to-copolarization power ratios with respect to the reflectivity difference calculated from the Fresnel equations. Having the polarization-independent roughness model described by (10), we expect to have a roughness-free power distribution from (12). The power distributions, however, indicate wide variations around the dashed line in Fig. 9(c), i.e., the line of the reflectivity difference. This indicates the polarization-dependence of the roughness effect.

The plots of Fig. 10 show the estimates of noise power calculated from the quadrature component of the zenith-looking antenna [15]. As can be seen in Fig. 10(a), higher noise powers occur at lower elevation angles where the power of copolarization reflection is prominently high. This makes the tracking of the direct signals more difficult compared to higher elevation angles where both the reflectivity power loss (see Fig. 7) and roughness effect suppress the reflection power. Fig. 10(b) presents the statistics of noise power estimates against different wind speeds. No prominent dependence on sea state can be observed in the variations of noise power described by the standard deviation values. The unaffected noise power here in a coastal setup is in contrast to sea-

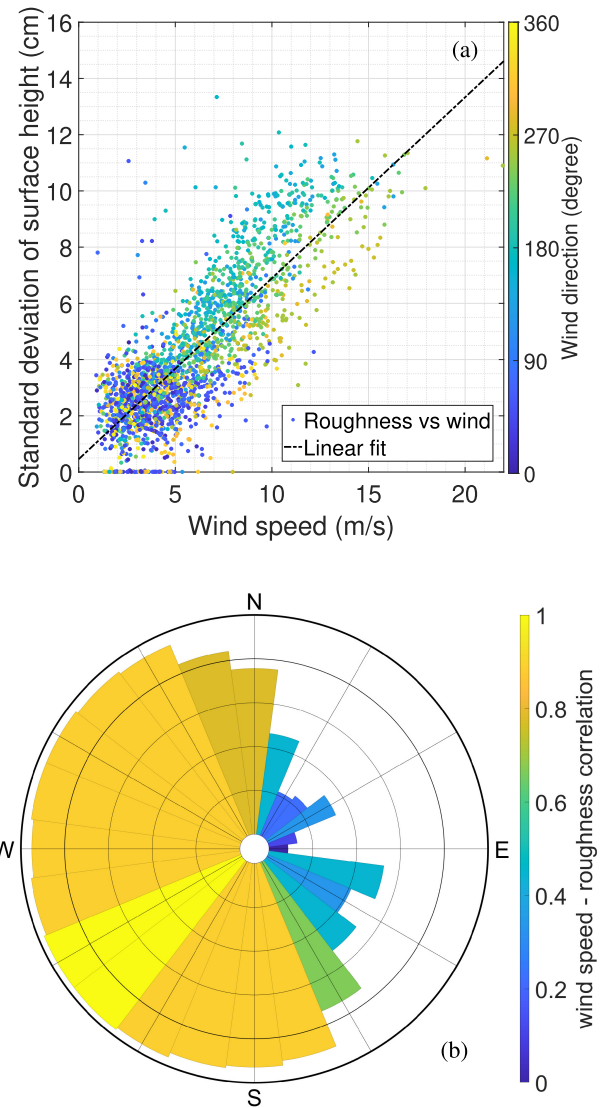


Fig. 14. Results of the full polarimetric roughness retrievals based on the one-year GNSS-R measurements in 2016. (a) Roughness estimates against different wind speeds overlaid with the first-order polynomial. (b) Dependence of the roughness retrievals on the direction of wind fields.

state-dependent noise from the ship measurements described in [15]. However, an insignificant rise of noise power with the increasing wind speed can be seen in our measurements.

The level-2 product of SSR measurements against different wind speeds and wind directions is depicted in Fig. 11. The standard deviation of surface height is the measured parameter describing the SSR. In general, the anomalies of the roughness estimates derived from the copolarization and cross-polarization observations are well connected to the variations of wind speed. The overall correlations of the roughness products with wind speed are about 0.76 for the copolarization and cross-polarization links. However, an analogy between the behavior of the results in Fig. 11(a) and (b) reveals noticeable discrepancies.

Fig. 11(a) includes observations that are mapped to zero-roughness. This is particularly the case for most of the winds blowing from  $0^\circ$  to  $90^\circ$  azimuth angles. Besides, the roughness measurements in the figure exhibit wind direction dependence



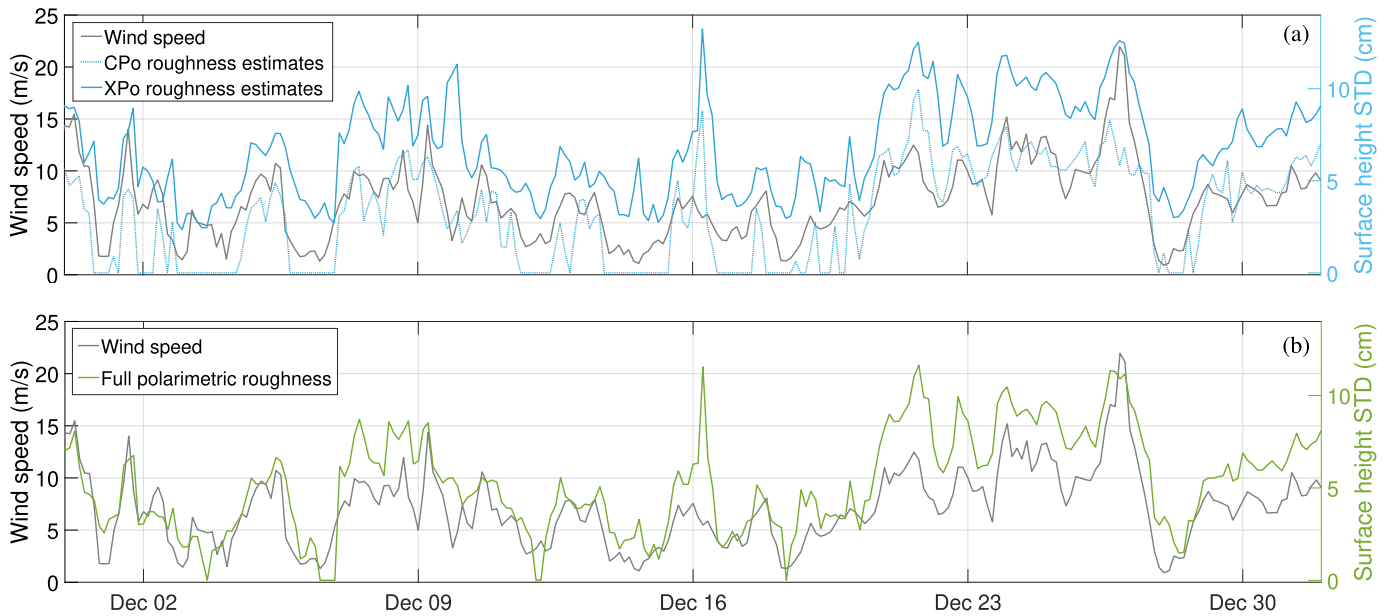


Fig. 15. Exemplary time series of SSR estimates from GNSS-R measurements in December 2016. (a) Roughness retrievals from the copolarization (CPo) and cross-polarization (XPo) measurements. (b) Roughness retrievals from a full polarimetric solution, i.e., combination of CPo and XPo measurements.

patterns. A bias can be seen in the copolarization measurements, which indicates that the corresponding observations are mostly not responsive to the wind speeds below 2 m/s. The values of  $\sigma$  derived from the copolarization link are mainly below 9 cm.

The roughness estimates from the cross-polarization antenna present better performance compared to the copolarization link. The distribution of the roughness retrievals against different wind speeds shows a higher sensitivity of cross-polarization measurements to the sea state.

The dependence of the roughness retrievals to the wind direction can be distinguished from the clustered pattern in Fig. 11(b). The lowest dependence can be seen for the north to the east winds. In contrast, south and west winds have triggered clearer responses in the results. As can be seen in the figure, the linear fit to the data reveals a bias in the roughness retrievals, which could be partly attributed to the signal processing procedure in the receiver. The signals received by the two sea-looking antennas are processed within two separate channels. Therefore, different Automatic Gain Controller (AGC) factors are applied to the received signals. In the calculation of cross-polarization ratios (11), the reference power of the direct signal is estimated from the copolarization link. Therefore, the cross-polarization power ratios could be affected by different AGC values. This bias is shown more clearly in the cross-to-copolarization roughness measurements [see Fig. 11(c)]. The retrievals shown in Fig. 11(c) present an overall correlation of about 0.35 with wind speeds despite the expectation of having almost no correlation. This implies that the effect of roughness in the cross-polarization observations is more pronounced.

The mean absolute errors associated with the roughness retrievals are listed in Table I. The error estimates are calculated based on the residuals of the optimized solution for (13). The retrievals from the cross-polarization link are associated

TABLE I  
MEAN ABSOLUTE ERROR VALUES ASSOCIATED WITH  
THE ROUGHNESS RETRIEVALS SHOWN IN FIG. 11

		wind speed range (m/s)			
	power ratios	0-5	5-10	10-15	>15
mean	co-polarization	3.9	3.7	4.2	5.6
absolute	cross-polarization	3.1	3.1	3.9	5.7
error (dB)	cross to co-polarization	3.7	3.8	3.9	3.8

with smaller error values. However, the errors increase with the rise of wind speed for the copolarization and cross-polarization roughness retrievals.

The impact of wind direction on the roughness retrievals is shown in Fig. 12. The correlation of the retrieved SSR with the direction at which the wind is blowing is shown in a polar coordinate system. The copolarization and cross-polarization roughness estimates are highly correlated with the winds blowing from the range of south-southeast to north, i.e., from  $150^\circ$  to  $360^\circ$ . The winds with the directions falling in the range of  $10^\circ$ – $90^\circ$  are almost ineffectual to produce strong responses in the observations.

The different performance of the roughness retrievals with respect to the wind direction can be related to the location of the station. From the wind distribution shown in Fig. 3(a), it can be recognized that the north–northeast wind is a major direction of the wind in this area. However, this direction and the wind fields with the direction from  $15^\circ$  to  $135^\circ$  do not stimulate prominent roughness in the sea surface. When the wind is blowing from land, i.e., during the “offshore or land breeze,” there is no fetch for wind-driven waves at the coast. Thus, the roughness will not increase. Using wind speed ancillary data as a proxy for roughness may be difficult in fetch-limited areas. Roughness and wave spectrum are also constrained by shallow water in coastal areas. The coastal effect on roughness is observed in synthetic aperture

radar (SAR) data [20] and is well known in the ocean wave modeling community [21]. Conditions change when the wind is blowing from the sea (south, west, and north–west). Winds from these directions, i.e., the “onshore or sea breeze,” can produce developed sea states and, thus, maximal roughness. However, even the roughness developed by these winds could be suppressed by the complex coastlines surrounding the station and nearby small islands. Fig. 13 shows three regions with different sea states. The developed sea state in region C is partly transferred to region B, and a calmer condition can be seen in region A compared to the regions B and C.

We combine the observations from the two sea-looking antennas to assess the performance of a full polarimetric solution to (13). The results are presented in Fig. 14. The full polarimetric roughness estimates have an overall correlation of about 0.82 with wind speeds. The results manifest almost no bias compared to Fig. 11(a) and (b). Fig. 14(b) reports on the improved sensitivity to wind-driven roughness for all wind directions. The figure shows that the roughness responses to the wind fields from the azimuth of  $165^\circ$  to  $345^\circ$  are almost entirely identified by the polarimetric GNSS-R observations.

Fig. 15 demonstrates exemplary time series of the reflectometry-derived SSR from the copolarization and cross-polarization power ratios in December 2016. Both the time series in Fig. 15(a) represent high correlations with the wind speed variations. Fig. 15(b) illustrates the time series of full polarimetric roughness estimates with enhancements compared to the copolarization and cross-polarization time series.

## V. CONCLUSION

We have investigated the response of GNSS reflectometry observations to the SSR during different wind conditions. A coastal GNSS-R experiment has been used to assess the performance of polarimetric observations for estimating the roughness. Two sea-looking antennas with copolarization and cross-polarization designs with respect to the polarization of incoming direct signals are used in the experiment. The processing results from both antennas show successful roughness retrievals over the one-year period of the analyzed data set. However, stronger manifestations of the SSR can be seen in the cross-polarization measurements. The left- and right-handed polarized components of reflected signals are affected differently by SSR. Wind speeds as low as about 1 m/s are detected in cross-polarization retrievals, whereas significant copolarization retrievals occur mainly for wind speeds above 2 m/s. The effect of sea state can be seen in the cross-to-copolarization power ratios, which is not expected. This reveals the need for an enhancement in the state-of-the-art model. A clear dependence on the wind direction, due to different fetch lengths and the nearby complex coastlines, is observed in the roughness estimates. The winds blowing from the open-sea areas have shown the maximal impact on the roughness values compared with the winds blowing from land. A full-polarimetric solution has been also tested for roughness retrieval. The results show noticeable improvements compared to the copolarization or cross-polarization results.

The full-polarimetric retrievals show an increased sensitivity to wind speeds from all directions.

## ACKNOWLEDGMENT

The authors would like to thank Dr. Georg Beyerle for his scientific comments. The Swedish Meteorological and Hydrological Institute (SMHI) and the Onsala Space Observatory (OSO) are, respectively, acknowledged for the ancillary data and hosting the experiment.

## REFERENCES

- [1] H. Zhang *et al.*, “Observation of sea surface roughness at a pixel scale using multi-angle sun glitter images acquired by the ASTER sensor,” *Remote Sens. Environ.*, vol. 208, pp. 97–108, Apr. 2018.
- [2] V. U. Zavorotny and A. G. Voronovich, “Scattering of GPS signals from the ocean with wind remote sensing application,” *IEEE Trans. Geosci. Remote Sens.*, vol. 38, no. 2, pp. 951–964, Mar. 2000.
- [3] C. S. Ruf *et al.*, “A new paradigm in Earth environmental monitoring with the CYGNSS small satellite constellation,” *Sci. Rep.*, vol. 8, no. 1, pp. 1–13, Dec. 2018.
- [4] M. Hoseini, M. Asgarimehr, V. Zavorotny, H. Nahavandchi, C. Ruf, and J. Wickert, “First evidence of mesoscale ocean eddies signature in GNSS reflectometry measurements,” *Remote Sens.*, vol. 12, no. 3, p. 542, Feb. 2020.
- [5] A. Camps, X. Bosch-Lluis, I. Ramos-Perez, J. F. Marchan-Hernandez, B. Izquierdo, and N. Rodriguez-Alvarez, “New instrument concepts for ocean sensing: Analysis of the PAU-radiometer,” *IEEE Trans. Geosci. Remote Sens.*, vol. 45, no. 10, pp. 3180–3192, Oct. 2007.
- [6] J. F. Marchan-Hernandez *et al.*, “Sea-state determination using GNSS-R data,” *IEEE Geosci. Remote Sens. Lett.*, vol. 7, no. 4, pp. 621–625, Oct. 2010.
- [7] F. Soulat, M. Caparrini, O. Germain, P. Lopez-Dekker, M. Taani, and G. Ruffini, “Sea state monitoring using coastal GNSS-R,” *Geophys. Res. Lett.*, vol. 31, pp. 1–4, 2004, Art. no. L21303, doi: 10.1029/2004GL020680.
- [8] E. Cardellach, S. Ribó, and A. Rius, “Technical note on Polarimetric phase interferometry (POPI),” 2006, *arXiv:physics/0606099*. [Online]. Available: <https://arxiv.org/abs/physics/0606099>
- [9] A. Egidio *et al.*, “Airborne GNSS-R polarimetric measurements for soil moisture and above-ground biomass estimation,” *IEEE J. Sel. Topics Appl. Earth Observ. Remote Sens.*, vol. 7, no. 5, pp. 1522–1532, May 2014.
- [10] D. Schiavulli, A. Ghavidel, A. Camps, and M. Migliaccio, “GNSS-R wind-dependent polarimetric signature over the ocean,” *IEEE Geosci. Remote Sens. Lett.*, vol. 12, no. 12, pp. 2374–2378, Dec. 2015.
- [11] E. Motte *et al.*, “GLORI: A GNSS-R dual polarization airborne instrument for land surface monitoring,” *Sensors*, vol. 16, no. 5, p. 732, May 2016.
- [12] A. M. Semmling *et al.*, “A zeppelin experiment to study airborne altimetry using specular global navigation satellite system reflections,” *Radio Sci.*, vol. 48, no. 4, pp. 427–440, Jul. 2013.
- [13] Y. Zhou, R. H. Lang, E. P. Dinnat, and D. M. Le Vine, “L-band model function of the dielectric constant of seawater,” *IEEE Trans. Geosci. Remote Sens.*, vol. 55, no. 12, pp. 6964–6974, Dec. 2017.
- [14] R. Lang, Y. Zhou, C. Utku, and D. Le Vine, “Accurate measurements of the dielectric constant of seawater at L band,” *Radio Sci.*, vol. 51, no. 1, pp. 2–24, Jan. 2016.
- [15] A. M. Semmling *et al.*, “Sea-ice concentration derived from GNSS reflection measurements in Fram Strait,” *IEEE Trans. Geosci. Remote Sens.*, vol. 57, no. 12, pp. 10350–10361, Dec. 2019.
- [16] W. Liu *et al.*, “Coastal sea-level measurements based on GNSS-R phase altimetry: A case study at the Onsala space observatory, Sweden,” *IEEE Trans. Geosci. Remote Sens.*, vol. 55, no. 10, pp. 5625–5636, Oct. 2017.
- [17] K. M. Larson, E. E. Small, E. Gutmann, A. Bilich, P. Axelrad, and J. Braun, “Using GPS multipath to measure soil moisture fluctuations: Initial results,” *GPS Solutions*, vol. 12, no. 3, pp. 173–177, Jul. 2008.
- [18] F. G. Nievinski and K. M. Larson, “Forward modeling of GPS multipath for near-surface reflectometry and positioning applications,” *GPS Solutions*, vol. 18, no. 2, pp. 309–322, Apr. 2014.
- [19] E. Cardellach, F. Fabra, A. Rius, S. Pettinato, and S. D’Addio, “Characterization of dry-snow sub-structure using GNSS reflected signals,” *Remote Sens. Environ.*, vol. 124, pp. 122–134, Sep. 2012.

- [20] M. A. Sletten and P. A. Hwang, "The effect of wind-wave growth on SAR-based waterline maps," *IEEE Trans. Geosci. Remote Sens.*, vol. 49, no. 12, pp. 5140–5149, Dec. 2011.
- [21] *Shore Protection Manual*, Dept. Army, Waterways Exp. Station, Corps Eng., CERC. (US), Vicksburg, MS, USA, 1984.



**Mostafa Hoseini** graduated in geodesy from the University of Tehran, Tehran, Iran. He is pursuing the Ph.D. degree with the Norwegian University of Science and Technology (NTNU), Trondheim, Norway.

He worked for several institutions as a GNSS Engineer in the field of positioning and navigation. He worked on the analysis of GNSS atmospheric products with the German Research Center for Geosciences (GFZ), Potsdam, Germany. His research interests include GNSS-based remote sensing techniques and sensors. His research focuses on the monitoring of the ocean and Arctic using the GNSS-reflectometry sensor onboard small satellites.



**Maximilian Semmling** graduated in physics from Leipzig University, Leipzig, Germany, in 2007, and the Ph.D. degree from Technische Universität Berlin, Berlin, Germany, in 2012.

For his doctoral and post-doctoral studies, he was with the German Research Center for Geosciences (GFZ), Potsdam, Germany, the Institute for Space Studies of Catalonia (IEEC), Catalonia, Spain, and the University of the Littoral Opal Coast (ULCO), Dunkirk, France. In 2020 he joined the Observation Department, German Aerospace Center (DLR), Institute for Solar-Terrestrial Physics, Neustrelitz, Germany. He is experienced in GNSS for Earth Observation with a research focus on ocean altimetry and sea ice remote sensing. His work concentrates on signal propagation effects for application in atmosphere sounding. Corresponding methods cover a wide range from ground-based measurements over maritime, airborne to satellite platforms.



**Hossein Nahavandchi** received the Ph.D. degree from the Royal Institute of Technology (KTH), Stockholm, Sweden, in 1998.

He is a Professor of Geodesy and Geophysics with the Norwegian University of Science and Technology (NTNU), Trondheim, Norway. His research interests involve global geodetic observations system (GGOS) including satellite gravimetry, satellite altimetry, satellite radar interferometry, and GNSS to understand the dynamic Earth system by quantifying Earth's change in space and time.



**Erik Rennspiess** was born in Pittsfield, MA, USA. He received the B.S. degree in environmental design with an emphasis on the built environment from the University of Massachusetts, Amherst, MA, USA, in 2013. He is pursuing the master's degree in geodesy and geoinformation science with the Technische Universität Berlin, Berlin, Germany.

His research interest includes GNSS remote sensing with a focus on ground-based GNSS-Reflectometry technique for monitoring coastal sea surface characteristics.



**Markus Ramatschi** received the Dipl.rer.nat. degree in geophysics and the Ph.D. degree in geophysics from the Technical University of Clausthal, Clausthal-Zellerfeld, Germany, in 1992 and 1998, respectively.

He is a Senior Scientist with the German Research Center for Geosciences (GFZ), Potsdam, Germany. His research interests include the operation of a global GNSS sensor station network.



**Rüdiger Haas** received the M.Sc. and Ph.D. degrees in geodesy from Bonn University, Bonn, Germany.

He is a Full Professor of space geodesy with the Department of Space, Earth and Environment, Chalmers University of Technology, Gothenburg, Sweden. He is the Head of the Research Group for Space Geodesy at Chalmers and responsible for the geoscience activities at the Onsala Space Observatory, Onsala, Sweden. His research interests focus primarily on space geodetic techniques, such as Global Navigation Satellite Systems (GNSS), including GNSS-reflectometry, and Very Long Baseline Interferometry (VLBI).



**Joakim Strandberg** received the M.Sc.Eng. degree in physics and the Ph.D. degree in radio and space science from the Chalmers University of Technology, Gothenburg, Sweden, in 2015 and 2020, respectively.

His research focuses on using reflected GNSS signals for remote sensing, especially for maritime purposes.



**Jens Wickert** received the Diploma degree in physics from Technical University Dresden, Dresden, Germany, in 1989, and the Ph.D. degree in geophysics/meteorology from Karl-Franzens-University Graz, Graz, Austria, in 2002.

He was the Principal Investigator of the pioneering GPS radio occultation experiment aboard the German CHALLENGING Minisatellite Payload (CHAMP) Satellite and coordinates numerous research projects on GNSS remote sensing. He holds a joint professorship of GFZ with the Technical University of Berlin on Global Navigation Satellite Systems (GNSS) remote sensing, navigation, and positioning. He is also the Deputy GFZ Section Head Space Geodetic Techniques and the GFZ Research Topic Director of The Atmosphere in Global Change. He has authored or coauthored more than 250 Web of Science indexed publications on GNSS Earth observation.